Journal of Volcanology and Geothermal Research 320 (2016) 19–28

Contents lists available at ScienceDirect

Journal of Volcanology and Geothermal Research

journal homepage: www.elsevier.com/locate/jvolgeores

A robotic approach to mapping post-eruptive volcanic fissure conduits

Carolyn E. Parcheta [a,*], Catherine A. Pavlov [b], Nicholas Wiltsie [a], Kalind C. Carpenter [a], Jeremy Nash [a], Aaron Parness [a], Karl L. Mitchell [a]

[a] Jet Propulsion Laboratory, California Institute of Technology, Pasadena, CA 91109, USA
[b] California Institute of Technology, Pasadena, CA 91125, USA

ARTICLE INFO

Article history:
Received 11 December 2015
Received in revised form 7 March 2016
Accepted 8 March 2016
Available online 26 March 2016

Keywords:
Hawaiian fountains
Fissure
Robots
Mapping
3D model

ABSTRACT

VolcanoBot was developed to map volcanic vents and their underlying conduit systems, which are rarely preserved and generally inaccessible to human exploration. It uses a PrimeSense Carmine 1.09 sensor for mapping and carries an IR temperature sensor, analog distance sensor, and an inertial measurement unit (IMU) inside a protective shell. The first field test succeeded in collecting valuable scientific data but revealed several needed improvements, including more rugged cable connections and mechanical couplers, increased ground clearance, and higher-torque motors for uphill mobility. The second field test significantly improved on all of these aspects but it traded electrical ruggedness for reduced data collection speed. Data collected by the VolcanoBots, while intermittent, yield the first insights into the cm-scale geometry of volcanic fissures at depths of up to 25 m.
VolcanoBot was deployed at the 1969 Mauna Ulu fissure system on Kīlauea volcano in Hawai'i. It collected first-of-its-kind data from inside the fissure system. We hypothesized that 1) fissure sinuosity should decrease with depth, 2) irregularity should be persistent with depth, 3) any blockages in the conduit should occur at the narrowest points, and 4) the fissure should narrow with depth until it is too narrow for VolcanoBot to pass or is plugged with solidified lava. Our field campaigns did not span enough lateral or vertical area to test sinuosity. The preliminary data indicate that 1) there were many irregularities along fissures at depth, 2) blockages occurred, but not at obviously narrow locations, and 3) the conduit width remained a consistent 0.4–0.5 m for most of the upper 10 m that we analyzed.

1. Introduction

Robots have evolved over the last several decades as an excellent means of collecting scientific data. They can often access locations of interest that are either too dangerous or too difficult for humans to explore. *Mars* rovers from the National Aeronautics and Space Administration (NASA) exemplify this case, making numerous discoveries about the geologic history and habitability of the red planet (Squyres and Knoll, 2005). On Earth, several robotic platforms have been used to explore steep slopes and caves. These field campaigns collect valuable scientific data that help explain the geology and biota of our own planet, and they serve as a proving ground for technologies that can be used in future missions to explore other destinations in the solar system. Several wheeled robots have been demonstrated on Earth with exploration strategies similar to those of the Mars rovers (Sutoh et al., 2012) including RoboVolc (Muscato et al., 2013), Zoe (Wettergreen et al., 2005), and the ROCKY series of robots from JPL (Volpe et al., 1997). Several researchers have also used remotely controlled aerial platforms to survey these field sites (Nagatani et al., 2013; Yajima et al., 2014).

1.1. Motivation

There are two reasons for robotically descending into volcanic conduits:

1) Data are sparse (Section 2.2) on a detailed sub-1 m scale for geometry of volcanic conduits. Such data would significantly enhance our understanding of volcanic eruption dynamics, and
2) Subsurface human access to the field site exposure (Section 2.3) is commonly impossible due to narrow widths, unknown depths, and rough glassy walls; for the Mauna Ulu fissure described in this paper, human entrance is not allowed by the National Park Service.

A robotic platform offers the ideal entry solution for the fissure system. The platform's mobility expands its mapping capabilities over that of an instrumented plumb bob. This prompted the concept, construction, and deployment of VolcanoBot, a small, rotary, tethered robot for navigating and documenting near-vertical surfaces.

* Corresponding author.
E-mail address: carolyn.e.parcheta@jpl.nasa.gov (C.E. Parcheta).

http://dx.doi.org/10.1016/j.jvolgeores.2016.03.006
0377-0273/

2. Background

2.1. Robotics

Since the late 1990s, several robots have been built to navigate steep or vertical rock faces for scientific purposes — some specific to volcanoes and others to caves. The first tethered robot to explore steep surfaces was Dante (Bares and Wettergreen, 1999), which used a legged architecture to descend 165 m into Mt. Spurr's central crater to collect fumarolic gas samples. The TERESSA system used two cables to descend steep slopes in Svalbard, which allowed the robot to move side to side to targets of interest on the cliff side (Huntsberger et al., 2007). More recently, the AXEL platform used a single rappel line to descend steep slopes (Nesnas et al., 2012). AXEL can carry scientific instruments in its wheel bays and has demonstrated a small coring drill (Nesnas et al., 2012). Robots from Carnegie Mellon University (Huber et al., 2014) use a series of cables spanning large crater entrances to traverse across the open surface mine and subsequently rappel into the excavated area. The LEMUR robot also accesses cliff faces and the ceilings of caves, but does so without a tether by climbing the rock walls with microspine grippers (Parness et al., 2013).

This work presents VolcanoBot (Fig. 1), a miniaturized platform that can access narrow fissure systems inaccessible to previous generations of steep-surface rappelling robots. VolcanoBot also leverages recent advances in 3D mapping sensor technologies to map the underground voids with high accuracy using a low-cost PrimeSense Carmine 1.09 sensor. Wong et al. provide a good comparative analysis of ranging mapping sensors (Wong et al., 2011). VolcanoBot's use of the PrimeSense was driven by the need for volume constraints, low cost, and the availability of open-source processing software. An overview of Infrared (IR) sensor systems and their application to robotics can be found in El-laith et al. (2012).

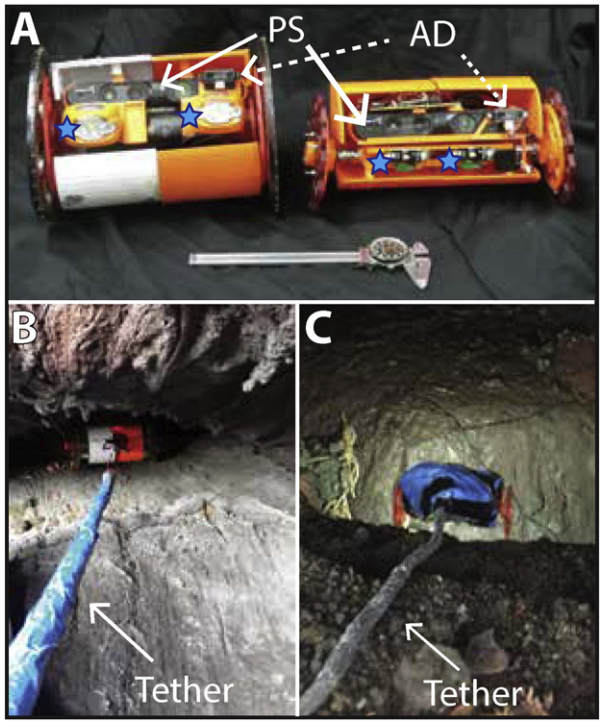

Fig. 1. A. Front view of VolcanoBots 1 (left) and 2 (right). PrimeSense (PS) Carmine 1.09 sensors are the long black cameras with three lenses (solid arrows). Analog distance sensors (AD) are the small black boxes on the right side of each robot (dashed arrows). LED headlamps (blue stars) were removed from their casing on VolcanoBot2, but are the same product as on VolcanoBot1. B. VolcanoBot1 and C. VolcanoBot2 descending into fissures.

VolcanoBot data are post-processed in two free, open source programs called Kinect Fusion (Point Cloud Library, 2014; Izadi et al., 2011; for creating point clouds and their surface textures, i.e., a "mesh") and Meshlab (Cignoni et al., 2008; for manipulating point clouds and surface meshes). Our team is currently using these point clouds as inputs to fluid dynamics simulations of volcanic fissure eruptions, accounting for the non-vertical and non-linear geometries of fissures for the first time.

2.2. Volcanology

During volcanic unrest, a dike can propagate (Delaney et al., 1989) through a volcano and produce a fissure eruption when it intersects the ground surface. During this type of eruption, magma generally erupts simultaneously out of many vents located along the eruptive fissure's extent. Fissure eruptions are the most common eruption style (Macdonald et al., 1983) and are the low-intensity end member of the sustained explosive volcanic eruption spectrum (Walker, 1973). Lava fountains erupting from fissure vents typically have heights <100 m (Fig. 2), and the fissure systems are typically ≥1 km in length.

Precise, subsurface, conduit geometries are currently unknown. State of the art geologic practice can resolve large-scale volcanic conduits and storage zones (10s–100s of m) with earthquake patterns (Almendros et al., 2002), ground deformation studies (Poland et al., 2006), and muon radiography (Tanaka et al., 2007). While the volcanological community ideally desires detailed meter-scale or better observations, these measurements are impossible to make during an eruption because of associated hazards (lava flows, intense heat, toxic gas, pyroclastic fall out). This has caused simplifications to be adopted in models that address volcanic eruption dynamics and inform hazard assessment studies. With the technological advances of recent years, obtaining precise knowledge on conduit geometries is now a key stepping-stone in volcanology over the next 100 years (Poland, 2015). The first detailed studies of shallow fissure conduits (<5 m deep) and vents (Parcheta et al., 2015) documented that geometries are tens of centimeters to 5 m wide and 1 m to tens of meters long within 5 m of the ground surface. By robotically measuring the 3D geometries of deeper exposed conduits, our research program aims to increase our understanding of how volcanic conduit geometries evolve and control eruption dynamics.

2.3. Field environment

The initial fissure of the 1969–74 Mauna Ulu eruption of Kīlauea volcano in Hawai'i (Swanson et al., 1979; Tilling et al., 1987) (Fig. 3) was active for 18 h on May 24, 1969. Manu of the vents along the western part of the fissure system were not destroyed or buried by lava flows during the eruption, providing a good opportunity to document these features in detail. The fissure is lined with moderately vesicular basalt; very thin shelly pāhoehoe rinds are common around vent surfaces with lava drain-back features (Parcheta et al., 2012). There is no geological or geophysical evidence that the fissure has been significantly altered since 1969 (Swanson et al., 1979; Tilling et al., 1987; Parcheta et al., 2012). A nearby fault scarp superficially resembles the fissure, but the face of the scarp is composed of weathered, low to moderately vesicular, basaltic lava flows that are 1–3 m thick. The fault scarp, part of the Koa'e fault system (Fisk and Koyanagi, 1968), has a different formation time than the fissure and did not erupt magma at any time (Swanson et al., 1979; Parcheta et al., 2012). We mapped this feature to facilitate a textural and waveform comparison to the fissure system.

3. VolcanoBot design

Gaining access to any depth of an eruptive volcanic conduit is both rare and technologically difficult. By assuming that fissure surface vent dimensions reflect the largest possible size of fissure conduit (Wylie

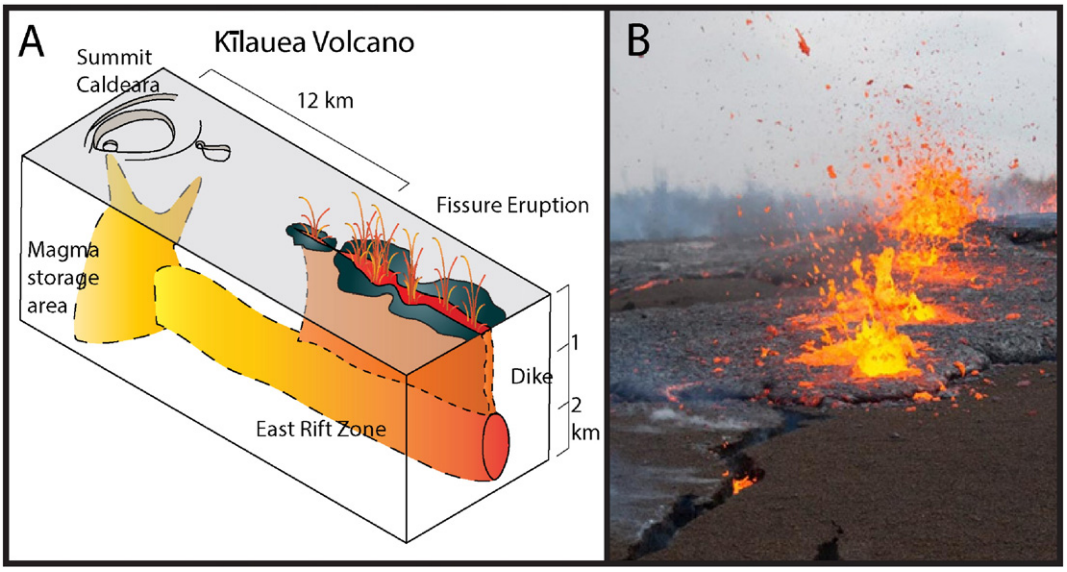

Fig. 2. A. Schematic of the general relationship between Kīlauea's magma chamber, dikes, and eruptive fissures. B. Example of a fissure eruption, the 2011 Kamoamoa eruption, Kīlauea. The direction of propagation is toward the photographer. The crack in the foreground is ~30 cm wide. Photo courtesy USGS.

et al., 1999), we can constrain the size of the instrument(s), type of mobility, and tether management required for a robotic platform to map the fissure system.

3.1. Platform

The design goal of the robot was mobility inside a vertical crack-like geometry of unknown surface irregularity and variable width. Several constraints immediately narrowed the platform design down to one option.

First, due to the narrow nature of the fissure and desire to transcend 10s of meters quickly, we deemed legged mobility infeasible. It is also difficult to construct multi-legged robots with several degrees of freedom on a very small (<30 cm) scale. Knowing that the walls were likely rough meant that a legged system would require a large number of joints per limb and an advanced sensing and autonomy system to plan footfalls. This type of system is more suited to robots of much larger size.

Second, the near-vertical ($\pm 30°$) orientation of the fissure necessitated a platform designed to rappel and climb, with horizontal mobility being a secondary priority. This drove a rotary architecture (two wheels with a reaction tail) with a rappel line attached to the end of the tail. Adding a second axle to the system (tricycle or 4 wheel configuration) stabilizes the sensor head on regular terrain, but couples the tension in the rappel line to the pitch angle of the robot on rough terrain where one axle may make contact while another is off the surface, and where the tether line may take a tortuous path into the fissure. Additionally, the possibility of overhangs being encountered led to the need for wheels that are larger than the sensor platform so that the robot would be mobile whether it was inverted or remained right side up.

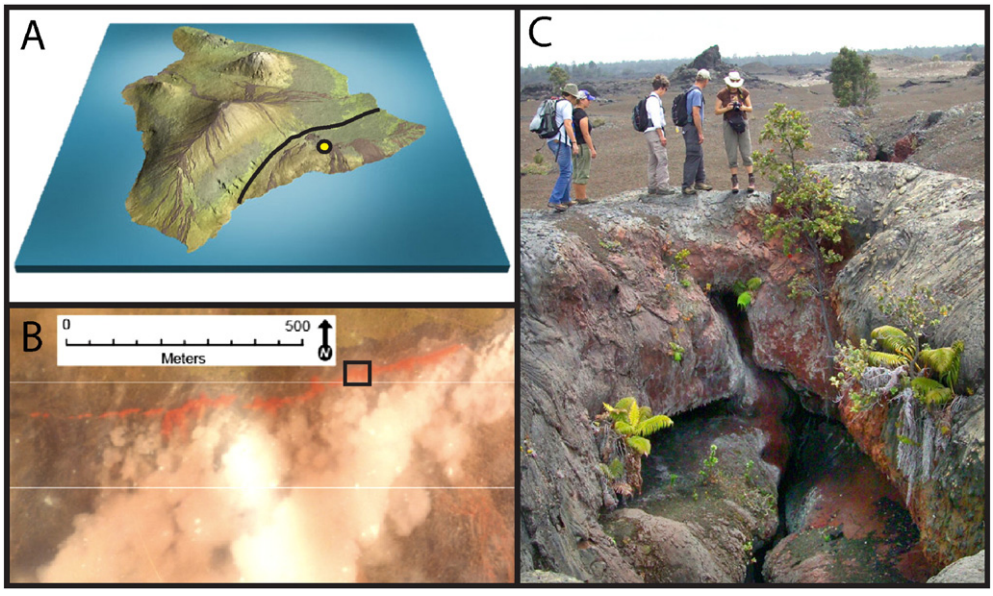

Fig. 3. A The island of Hawai'i. Yellow circle is the Mauna Ulu field site on Kīlauea volcano (south of black line). B. Aerial photograph taken by Sandia Laboratories of the fissure erupting in 1969. Black box indicates panel C. Photo courtesy of the USGS. C. Vent 47 on the Mauna Ulu fissure, and the location of our target priority vent for the VolcanoBot1 mapping campaign.

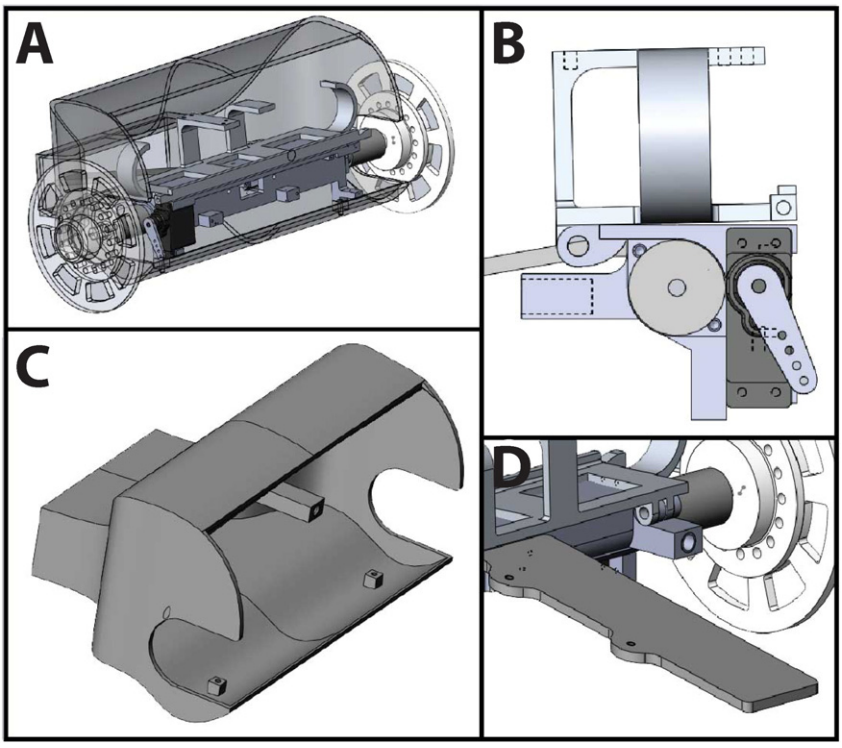

Fig. 4. Computer-aided drawing of VolcanoBot2 components. A. Fully assembled with the shell shown as a transparent layer. Improved version consists of 4 parts to carry the instrument and electronic payload: the body platform, wheel adapter, tail, and protective shell. B. Body platform consists of a hinged piece where the top half (light blue) is the Carmine 1.09 harness and the bottom half (medium blue) is the Maxon motor and light harness, with a servo (dark gray and blue) to control the Carmine 1.09 mount. C. Protective shell, attachment points protruding into the robot from the back of the shell secure the shell to the body platform. D. Tail and wheel adapter. The tail (dark gray) has 2 mounting holes for the RPi. Two wheel adapters (white) are used on the robot: they allow the motors to securely attach to the cast wheels, providing maximum transfer of power for mobility.

The third major design constraint was the need for stability in a vertical orientation. The sensor package needed to be compact and symmetrical to maintain stability on the wall and keep the sensor pointed down the fissure with both walls in the field of view. The mass was kept as close to the wall as possible while leaving enough ground clearance (~5 cm) to roll over roughness on the wall so that the robot does not become stuck (or grounded) on the wall.

As a result of these constraints, a two-wheeled design with rock-climbing wheels was chosen for its small size, simple functionality, and ease of modification. The second iteration of the robot has a reduced size (Fig. 4), weight, and tether diameter while at the same time having increased wheel power, field of view, robustness, and maneuverability (Table 1). Additionally, the housing for the instruments can actively rotate up to 30° using a servomotor to gain better viewing angles for the sensors inside the fissure.

3.2. Instrument suite

Both versions of the VolcanoBot carry the same 4-instrument payload: a PrimeSense Carmine 1.09 sensor for 3D visualization, a short-range analog distance sensor, an infrared temperature sensor, and a MiniIMU. The Carmine 1.09 sensor has dimensions 7 cm ×

Table 1
Summary of VolcanoBot 1 and 2 design specifications.

Specifications		Version capability	
Category	*Parameter*	*VolcanoBot1*	*VolcanoBot2*
Platform	3D printed harness	Y	Y[a]
	Shell size	14 cm	12 cm
	Length	30.5 cm	25.4 cm
	Weight without tether	1386 g	872 g
Mobility	Wheel diameter	17.5 cm	12.5 cm
	Motors	Recon Scout XT	Maxon, brushed motor
	Wheel torque	0.39 N ∗ m	1 N ∗ m
CPU	Available processing and data storage	N	Raspberry Pi B+ interface
Instrument payload	Carmine 1.09 (RGB and 0.5–3 m IR depth)	Y	Y
	Analog distance (10–80 cm)	Y	Y
	IR temperature	Y	Y
	MiniIMU	Y	Y
	Lights	Y	Y
Tether bundle	Mechanical tether 1/16″ steel cable	Y	Y
	Electrical cords	3	1
	Outer sheath	Wrap around braided sleeving	Wrap around vinyl coated cleaving

Y = yes, N = no.
[a] Harness is hinged and printed as 2 pieces instead of 1.

2 cm × 1.5 cm, and has a range of 0.5 m to 3 m (Konolige and Mihelich, 2012; PrimeSense 3D sensor datasheet), which is ideal for fissure geometries where walls are typically 0.5 m apart, but extend tens of meters into the ground. The analog distance sensor returns a reading within a 1.9 V analog voltage range corresponding to a 10–80 cm physical range (Sharp datasheet: GP2Y0A21YK0F, 2006). We use this distance sensor (3 cm × 1.3 cm × 1.4 cm) as a "visual braking mechanism" for VolcanoBot; we know the fissure is getting too narrow for safe passage when this sensor begins to register a signal. The IR temperature sensor determines ambient temperatures at 0.02 °C variations over −40–85 °C with a 0.5 °C accuracy (Melexis datasheet: MLX90612, 2008). This provides information on whether the fissure retains residual heat, or behaves more like a cave, adopting the mean annual temperature of the local climate. The MiniIMU is a 3-axis gyroscope and accelerometer (STMicroelectronis datasheet: L3G4200D, 2010), and provides orientation information for the robot, which is helpful during descent and will be used in the future to improve the feature-matching post-processing of the PrimeSense data.

We opted for the PrimeSense Carmine over a light detection and ranging system because of cost, size, minimum ranging threshold, and weight — all of which are limited on small expendable robots in narrow spaces. Parcheta et al. (2015) had previously attempted mapping the shallow conduit structure with lidar from the surface, but line-of-sight operation made it impossible to see past irregularities in the wall to any depth beyond the range of the human eye.

3.3. VolcanoBot1 apparatus

VolcanoBot1 was constructed around the commercially available Recon Scout XT (Recon Robotics Datasheet, 2011), which we utilized as the mobility system. A 3D-printed PLA harness was used to mount the instruments to the Recon Scout through its tail attachment points. Both the analog distance sensor and the Carmine 1.09 were mounted in fixed positions to the top of the Recon Scout XT in a forward-facing direction. We designed a printed circuit board (PCB) to communicate with the instruments, and mounted it behind the Carmine 1.09. The PCB contained the MiniIMU and temperature sensor. The Carmine 1.09 sensor was connected to a laptop at the ground surface via three 10-m-long USB booster cables. A powered USB hub inside VolcanoBot's shell provided the Carmine 1.09 sensor a direct 5 V power supply. The USB hub significantly increased the diameter of the robot, decreasing ground clearance to less than 3 cm. The 14 cm diameter protective shell is cylindrical in shape. Wheels attached on each end of the Recon Scout XT via laser-cut acrylic adapters and bellows-style couplers. Two 70-lumen headlamps were used to provide light for the RGB video feed. Data from the instruments were sent to the laptop via cat-6 Ethernet cable. The whole tether bundle, encased in a plastic mesh weave, included the USB booster cables, a power supply cable, the Ethernet cable, and a 1/16″ steel cable for mechanical strength.

3.4. VolcanoBot2 apparatus

VolcanoBot2 used two Maxon motors with high-torque planetary gearboxes for mobility. An ABS 3D-printed frame holds the motors and provides attachment points for the sensors and other circuitry. The instrument orientations remained similar to those of VolcanoBot1. VolcanoBot2 uses smaller 12.5 cm diameter wheels and, when combined with the new motors, has significantly more torque and mobility in the fissure. VolcanoBot2 was able to climb out of fissures on its own, provided that it was in contact with the wall and we gathered up the tether as it became slack. Shaft couplers that are smaller and rigid are used to attach the wheels in place of bellows-style flexible couplers to prevent shearing failures, which occurred during VolcanoBot1 tests. A mini computer known as a Raspberry Pi B+ (RPi; Raspberrypi Datasheet, 2014) is used to control the robot and record data from the PrimeSense, eliminating the USB booster cables, USB hub, and hub power cord from the system. The tether bundle is reduced to a single cat6 Ethernet cable and a 1/16″ mechanical steel cable tether. The RPi is mounted to the tail, and the shell is tapered to surround the Carmine 1.09, Raspberry Pi, and lithium polymer batteries. The ground clearance is 2.5 cm, and a servo motor can control the Carmine1.09 viewing angle by up to 30 degrees, allowing a view the opposing wall if the robot is tilted from the desired viewing position.

4. VolcanoBot fabrication

Both VolcanoBot platforms were constructed with three fabrication techniques. The main sensor harness and protective shell were 3D-printed with PLA or ABS plastic for rapid prototyping of sensor configurations and ease of design and fabrication. Molds for the wheels were milled out of wax blocks using a CNC machine. Hooks were then inserted into the wax and then over-molded with polyurethane. VolcanoBot1's wheels were designed to be semi-rigid, providing flexibility to conform to the fissure's roughness. VolcanoBot2's wheels were designed to be completely rigid and embedded with microspines (Parness et al., 2013) to allow it to climb.

5. VolcanoBot operations

5.1. Mechanical

Descent and ascent of VolcanoBot1 were manually controlled by feeding out or taking up the tether bundle while the data were recorded on a field laptop. The Carmine 1.09 sensor outputs two video feeds: the IR structured-light-derived depth map in a yellow-scale (Fig. 5A, online supplementary video), and an RGB visual feed. To map a given vent, the robot was positioned at 1-m intervals along the vent and allowed to descend by paying out tether and navigating with the live depth feed. This proceeded until either the full 30-m tether was deployed, the bottom of the fissure was reached, or an obstacle was encountered that could not be overcome, although intermittency in the USB signal from the booster cables also frequently ended runs.

Descent and ascent of VolcanoBot2 were controlled by a field laptop via an Ethernet cable. Commands were sent to the RPi, which in turn commanded a micro controller (called a Baby Orangutan) to drive the motors and collect the instrument data. The Carmine 1.09 and all instrument data were recorded directly by the RPi, with the Carmine video feeds being displayed on the field computer for navigation. Volcanobot2 can drive both into (down) and out of (up) the fissure. The limited processing speed of the RPi necessitated operating the robot at relatively slow speeds, pausing every 10–20 cm instead of moving continuously down the fissure walls.

5.2. Electrical

The PrimeSense Carmine 1.09 is VolcanoBot's primary mapping sensor for collecting three-dimensional fissure data. The sensor generates images of range measurements from a 7.5-cm baseline by projecting a laser-based, near-infrared structured light pattern to triangulate depth (Konolige and Mihelich, 2012). An infrared camera on the sensor acquires images of the structured light projection that the sensor's ASIC compares to a stored reference pattern at each pixel to determine depth from disparity (Konolige and Mihelich, 2012). The sensor provides VGA-resolution disparity images up to 30 frames per second with a depth range between 0.35 m and 1.4 m. The resolution is 0.1 cm at 0.5 m (PrimeSense Datasheet, 2013) after a linear algebraic transformation is applied to change the pixel disparity value into a depth (range) value (Point Cloud Library, 2014).

To construct a 3D model of the fissure (Fig.5C, online supplementary video), we integrate the range images from the Carmine sensor using Kinfu Large Scale, an open source implementation of the Kinect Fusion algorithm (Izadi et al., 2011). Kinect Fusion is a real-time, GPU-based

localization and mapping system for generating dense 3D reconstructions of a scanning area. Kinfu integrates depth measurements from the sensor into a truncated signed distance function (TSDF), which is a volumetric representation that implicitly represents surface geometry and sensor range uncertainty; the representation tracks sensor position by aligning consecutive sensor depth images (Izadi et al., 2011; Whelan et al., 2012). Kinfu Large Scale extends the original Kinfu implementation with a movable reconstruction volume that can scan unbounded environments. Overall map accuracy and camera position tracking are dependent on the scanned topography and sensor motion; rapid movements and geometrically featureless areas can cause ambiguity in matching range measurements and sensor position tracking loss. As a result of VolcanoBot's descent over rough surfaces, the point clouds are not continuous when processed through Kinfu but can be hand merged in Meshlab (Cignoni et al., 2008) to represent a continuous descent into the fissure.

6. Results

Table 2 summarizes the performance capabilities of VolcanoBots 1 and 2. Prior to deployment in the Mauna Ulu fissure system, both platforms were field tested in 2 environments at the Jet Propulsion Laboratory: on ≤40° slopes at Mars Yard (a Mars surface simulation facility) and on a 70° cobblestone wall.

6.1. VolcanoBot1 performance

During JPL tests, all instruments communicated with the field laptop and test data were successfully recorded. Mobility of the first platform was sufficient in flat, obstacle-free environments and descending environments at JPL, but the relatively large wheel diameter (to keep the wheels larger than the sensor package) decreased the torque available at the wheel for climbing and turning. Mobility of the robot around or over obstacles proved poor, limiting descents to near vertical transects.

In the Hawai'i field tests, several vents in the fissure system were successfully mapped. However, the electrical connections (USB hub and booster cables) between the Carmine 1.09 sensor and the laptop proved more fragile in this environment, frequently causing aborted runs or delays. The surface roughness of the fissure walls was a larger amplitude feature than that at JPL, causing the protective shell to be the only point of contact with the fissure wall in some locations (called high centering), and the wheels were of no use for mobility when this happened. As a result, a full view of both conduit walls during descent was rare. Since VolcanoBot1 had no instrument-pointing capabilities to offset the high centering, it could only document the wall that it was actively descending. Improved fissure views often came during the ascent phase when team members physically hoisted the robot out of the fissure. The mesh casing of the large tether bundle frequently snagged on the sharp rocks, causing the robot to stall until the tether was shaken free. This combination of challenges limited access to the full fissure system. Nevertheless, data collected by VolcanoBot1 during the Hawai'i field test were of high scientific value (discussed in sections 6.3 and 7.2) and provided a first-of-its-kind dataset.

6.2. VolcanoBot2 performance

A dozen JPL tests were conducted to iteratively test and run all instruments. The robot successfully communicated with the field laptop and test data were acquired, although the Raspberry Pi reduced the frame rate well below 30 fps. Mobility of this second platform was vastly improved with increased torque from the Maxon motors and a 5 cm reduction in wheel diameter. The robot could down-climb on all surfaces, and had little difficulty maneuvering across obstacles that VolcanoBot1 could not overcome. Volcanobot2 was able to turn ~30 degrees to the left and right on a 70° wall, and could turn 180° on a 40° slope. VocanoBot2 could also climb upwards (unassisted) on the 40° slope. For vertical faces, VolcanoBot2 could climb backwards up the walls provided that we pulled in slack on the tether as the robot climbed (otherwise it would flip itself over and fall off the wall).

In the Hawai'i field tests, the fissure system data set was expanded by mapping a nearby non-eruptive crack (for comparison) and another vent (vent 50, Parcheta et al., 2015) neighboring one of our previous vent locations (vent 47, Parcheta et al., 2015). The electrical connections of the second platform were more secure and reliable, but the write speed of the RPi did not improve in the Hawai'i test. As a result, the data were recorded at ~1/4–1/10 the original data rate of 30 htz (frames per second). There was a several-minute lag in the visual communications to the field laptop, which detrimentally slowed the pace of robotic deployment; consequentially, the onboard battery supply often died in the middle of data recording. The surface roughness of the fissure walls was no longer a hindrance with the improved ground clearance, yet an elevated center of mass often caused VolcanoBot2 to roll over and high center on the top portion of the shell, which extended slightly past the wheels. As a result, a full view of both conduit walls during descent was as rare as with VolcanoBot1; ascent provided the best views. The added instrument tilting mechanism worked well when VolcanoBot2 was right-side-up, but detracted from the visible range when VolcanoBot2 was up-side-down. The tether, now protected with vinyl-coated polyester sleeving, moved freely over the rock surface. It sustained many abrasive marks, but caused no failures or loss of signal.

6.3. Scientific results

VolcanoBot's design and deployment are aimed at addressing four hypotheses:

1) irregularities (protrusions on the fissure wall that alter the fissure's width) should persist with depth into the fissure because they are a result of the wall rock's fracture mechanical properties (Pollard, 1987),
2) fissures will have variable depths — i.e., locations that are blocked, whereas other portions remain open and navigable — because this is likely a function of lava solidifying in the narrowest spaces (Wylie et al., 1999),
3) fissures will likely narrow with depth and VolcanoBot will either become too large to access the bottom, or it will reach a false "bottom" where the fissure is completely blocked by solidified lava or rock fall.

Table 2
Summary of VolcanoBot 1 and 2 functional capabilities.

Specifications		Version capability	
Category	*Parameter*	VolcanoBot1	VolcanoBot2
Mobility	0° slope	Y	Y
	0° slope with obstacles	N	Y
	40° slope with obstacles	S	Y
	70° slope with obstacles	s	S
	90° slope, rough surface	s	S
	Driving mechanism	Either free descent/ascent/no turning, or RCF controller when in line of sight	Motorized descent/ascent/turning via laptop
Inst	Carmine viewing angle	Fixed, 54° × 47°	Adjust <45°, 54° × 47°

Y = yes, N = no, S = more semi-functional: could descend and turn, but not ascend, s = less semi-functional: could descend, but not turn or ascend.

4) fissure sinuosity (the deviation of the fissure system from a single line of strike) should decrease with depth because it is a function of the rotation in the surface stress field in the volcano, and no rotation is expected at depth (Pollard and Muller, 1976).

Although some technical difficulties arose with both VolcanoBots in Hawai'i, each was able to document and map the geometry of separate but neighboring parts of the Mauna Ulu fissure to depths of 10–25 m. VolcanoBot2 also documented a nearby fault for comparison with the fissure geometry. A full statistical analysis of these two geometries will provide a first step forward in understanding fissure eruption and initiation conditions. The initial results of the collected field data already give interesting insights into the Mauna Ulu fissure, and they begin to answer three of the four hypotheses.

Our first hypothesis, which the irregularities continue with depth into the fissure, is supported by the preliminary data. The walls are rarely "parallel and vertical" as in most fissure geometry models — they have irregularities (undulations) on them as far down as we were able to document in all of the videos. In a subset of the 3D reconstruction data that is <1 m wide (i.e. crack thickness), 3.5 m long, and 10 m deep (into the ground), there are 8 major irregularities in the wall. Preliminary measurements show the irregularities are 0.5–1.5 m long and 0.3–0.5 m wide (examples of two individual ones are shown in Figs. 5C and 6). Depth (i.e. vertical thickness) of the irregularities is difficult to constrain because the downward-looking PrimeSense Carmine 1.09 sensor is not able to document their undersides. We can constrain the maximum possible value for this dimension as being the vertical thickness observed plus the vertical distance of the data gap below the irregularity, but this is certainly an overestimate. The irregularities appear to be located at a ~2 m vertical spacing, but 8 data points are not statistically sound and more measurements will be made as the rest of the 3D data are assembled and analyzed. A horizontal spacing pattern is not apparent in the preliminary data thus far.

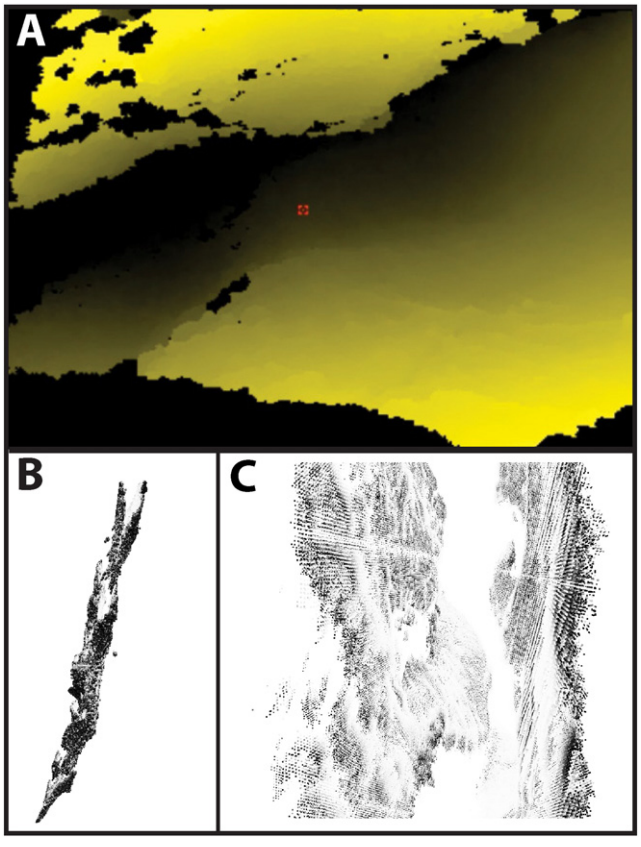

Fig. 5. Data collected from the Carmine 1.09 sensor during the May 2014 Hawai'i field test. A. IR-structured light raw depth image in yellow-scale. Black portions on the boundary of the image are too close to return a signal (less than 50 cm). Bright yellow indicates a 50 cm distance from the robot, and the yellow intensity fades as the distance increases. The black portion across the center of the image is beyond the range of the sensor (3 m). B. A cross-sectional view of a subset of the data, where the vent interface is in the upper right and the vent descends into the ground to the left of the image, and to the south in the field area. Image shows the top 5 m; "gap" in data in the middle part is the empty fissure. C. A zoomed-in view of the fissure point cloud, showing the south wall on the left, north wall on the right. Irregularities on the walls (large protrusions near center of image), are ~30 cm in diameter. See online supplementary videos corresponding to 5A and 5C.

Our second hypothesis involves several small blockages due to narrow conduit widths. The preliminary data partially support this hypothesis. The same <1 m × 3.5 m × 10 m subset of vent 47 has at least 2 small portions that are blocked from access; VolcanoBot1 could not navigate across them, but VolcanoBot2 was able to get around two of them. The videos from both platforms showed that the fissure extended deeper on either side of a blocked or clogged section (often topped with rubble debris). The first blockage is 5.5 m below the top of our model (9.5 m below the ground surface), and 2.5 m east of the western end of the vent. It has two large drainback features on either side that extend into the fissure below (Fig. 6, online supplemental video). The second blockage is midway across the length (4 m from either end) and is an apparent floor 10 m from the top of our model and 14 m below the ground surface. This rubbly floor was not seen in the western portion of the vent, and slopes downward in that direction. However, there is no obvious correlation between blockage locations and narrow conduit widths in the preliminary data.

Our third hypothesis concerns the eventual narrowing of the fissure, or a point at which there is a solidified floor. The preliminary data show no significant net narrowing of the fissure in the upper 10 m of our vent 47 model. There is an initial 1-m-deep section that slightly narrows from 0.8–0.4 m, followed by a quasi-constant 0.4 m width with some pinching and swelling due to the irregularities. This hypothesis will need more data over a greater depth range to be further tested. VolcanoBot1 robot did not reach the fissure's bottom in the western end of vent 47, indicating the fissure extends at least to 5 m beyond the visual reach of the Carmine 1.09 sensor. VolcanoBot2 documented a 15-m-deep, talus-filled section that may be the bottom of vent 50. Only once in the vent 47 subset did the fissure narrow to less than 20 cm where VolcanoBot1 could not pass; in vent 50, VolcanoBot2 was able to navigate laterally to a larger passage when the conduit was too narrow for it to move forward.

While below the size threshold of interest for this study, there were numerous vertical drip features on both walls throughout the area in vent 47 probed by VolcanoBot. These vertical drips are typically 1–2 cm wide, 3–6 cm long, and variable in length. Some drips have spherical ends, others pointed ends, and yet others fade back into the irregularity structure of the wall.

Our fourth, unaddressed hypothesis is that regarding sinuosity, a geometrical configuration that spans several vents (Parcheta et al., 2015). VolcanoBot was not able to go deep enough into the fissure or document a long enough length of the fissure (multiple vents) to fully address this hypothesis, and thus it will not be discussed further here.

7. Discussion

7.1. Robotic design functionality and interpretations

Significant improvements were made between the two VolcanoBot platforms. Most notable were the expanded mobility, reduced tether size and weight, with improved ability to slide over the rocks, more reliable electrical connections, a more compact design for tighter spaces, and the use of battery power over generator power. The ability to slowly climb upwards when in contact with the rock walls aided our retrieval of VolcanBot2 from the fissure's depths. The reduced size and weight of VolcanoBot2 and its tether made them easy to carry into the field in

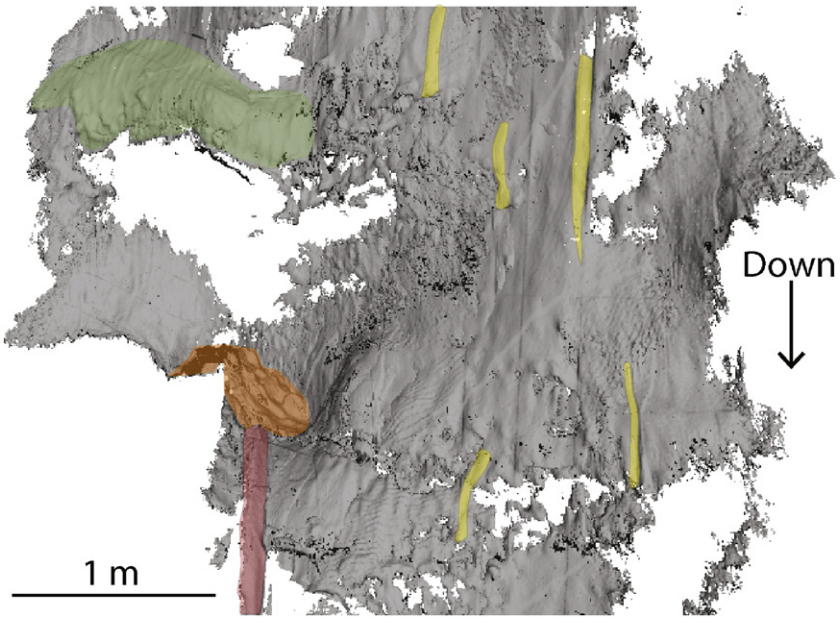

Fig. 6. Mesh image of the south wall of the fissure conduit in vent 47 (i.e. a surface layer created from the point cloud shown in Fig. 5B and C). See online supplementary videos corresponding to this figure for easier visualization. Green highlights an irregularity, below which is a data gap that constrains (and likely over-estimates) the maximum vertical dimension of the feature. The irregularity is 1.5 m long (left to right) and 0.3 m thick (into/out of the page, angling to the left). The orange feature below the irregularity is the talus-topped blocked section at 5.5 m depth and 2.5 m east of the western end of the vent. The talus is piled higher on the left side than the right. The red feature down from the talus is lava drainback, where lava was pouring off the blocked section as it solidified. The numerous yellow features highlight 6 of the drainback drip marks that coat the conduit walls, but several dozen can be seen in the image. These drips are cm scale in length (left to right) and width (into/out of the page), but extend for tens of cm to >1 m in depth along the conduit walls.

a backpack — effectively a one-person job for transporting the whole setup. Future versions of VolcanoBot now in development will expand upon these improvements.

The use of a Raspberry Pi as the main computer on the robot severely limited the operational pace due to its inability to process 30 fps from the PrimeSense. Future VolcanoBot platforms will migrate to more powerful mini computers and perhaps alternate mapping technologies to promote reliable, real time, and even more comprehensive, coverage of fissure conduits.

7.2. Scientific interpretations, discussion, and impact of VolcanoBot

Many of our interpretations are preliminary as the 3D model data are still being analyzed. However, with this caveat, some interesting interpretations are emerging. To a first order, Parcheta et al. (2015) interpreted the fissure conduit wall irregularities to have formed as a result of the host rock's fracture mechanics as the dike propagated toward the surface. That interpretation predicted that irregularities would thus persist with depth, and the robotic data show that they do. The preliminary results relevant to hypothesis 3 indicate that, because the fissure width remains quasi-stable for the lower 9 m of our model, each bulge is matched to a concave counterpart on the opposite wall — i.e. the irregularities appear to be piercing points, which are commonly used in determining how far a crack has opened and or moved laterally. Therefore, we not only infer that the irregularities at depth are an inherent feature of the wall rock, but also find that if they are piercing points, we can infer that the fissure opened as a Mode-I tensile crack (as described for dikes by Pollard (1987)), with minimal or no shear component. Interestingly, if this holds true as more data are added to the dataset, it would imply that anti-piercing points (two concave wall features directly opposite each other) may reflect syn-eruptive dynamical erosion (either mechanical or thermo-mechanical).

In considering the results of hypotheses 2 and 3, we find an increasing number of questions that will ultimately prompt our interpretations once more data are included. Preliminary findings are that the fissure does not narrow appreciably below the first 1 m of our model, yet short, rubble-topped blockages occur at 5 and 10 m depths. While we can infer that significant conduit narrowing likely did not play a role in the blockage formation, the question then remains as to what caused the blockage to form? Furthermore, was it there during the eruption, or did it form during the lava draining stage at the end of the eruption? These questions will need more data to be answered, but we can infer the following corollary based on our initial results. If conduit narrowing plays a role in forming syn-eruptive blockages, then there is likely a very small range of conduit widths (~<10 cm) in basaltic fissure conduits over which conditions change from allowing magma flow to being blocked. Other factors that must be addressed to properly interpret the origin of these blockages include: 1) determining if a narrow fissure would be observed at all, or if it would become obscured by the growing blockage, and 2) if these blockages formed after eruptive cessation (i.e. they were not present during the main eruptive activity), then what processes controlled the number and positions of lava fountains and what led to the successive waning of activity if the conduit was not becoming more and more blocked from cooling? The simple possibilities include running out of magma that can erupt through bubble nucleation and expansion or due to a hydraulic head effect, but more data is needed to distinguish these possibilities from each other.

We interpret the vertical “drip marks” on the conduit walls at all depths, and we interpret them as originating from the lava drainback at the end of the eruption. The spherical ends at the bottom of some drips indicate a downward direction of motion. In this data subset, drainback textures appear as cm–dm scale features, with fluid shapes, whereas irregularities appear as undulations in the wall at dm–m scales. As a result, we are optimistic that drainback textures and irregularities are distinctive, and one will not be misinterpreted for the other as this study progresses.

By using these geometries in models of eruption dynamics, we can begin to assess the feedbacks within the fissure's vents and how those feedbacks are displayed in lava fountains observed at the surface. As we finish analyzing this dataset, as well as expand it both deeper and to other terrestrial volcanoes, we will build a robust, second or third order dataset that can verify (or question) existing models of eruption

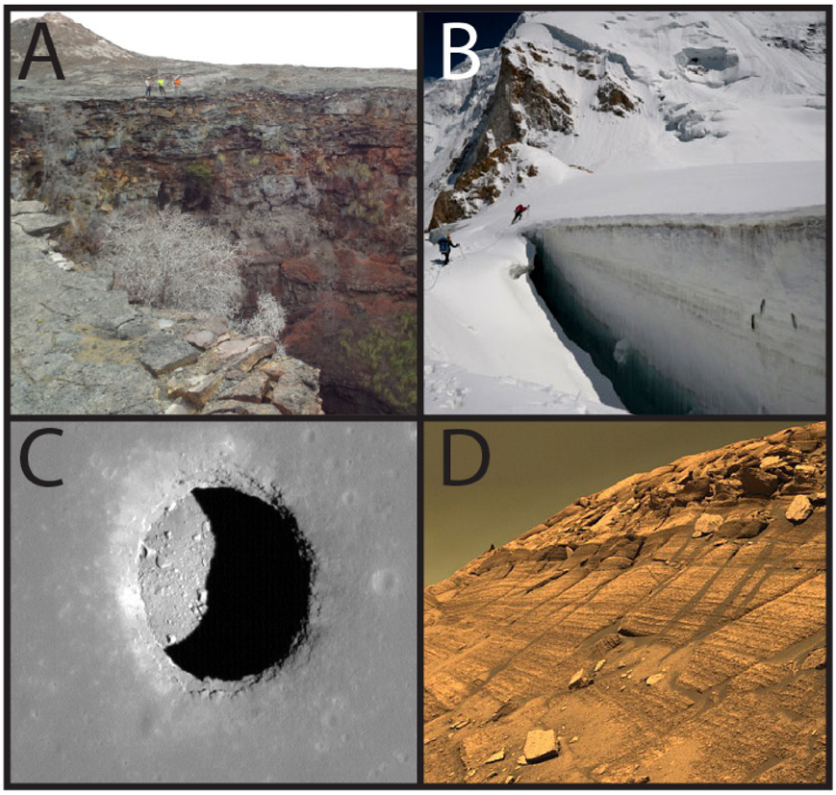

Fig. 7. Examples of potential future field sites for terrestrial and planetary applications. A: Volcanic pit craters. At Kīlauea, Hawai'i, 3 people are standing just left of center on the edge of the crater. B: Ice crevasses. Person for scale at left, and another at end of crevasse. Photo courtesy National Geographic. C: Collapsed feature in Mare Tranquillitatis on the Moon. Crater is ~100 m wide. Photo courtesy NASA. D: Burns Cliff, Endurance Crater, Mars. Photo courtesy of JPL/California Institute of Technology.

dynamics, magmatic flow within dikes, and the formation, spacing, and evolution of Hawaiian fountains.

7.3. Potential uses for terrestrial and extraterrestrial sites

VolcanoBot could be used as a capable and functional mapping tool in terrain geologically similar to fissures, such as:

- Geology — bedrock cliff faces, glaciers and ice crevasses, volcanic pit craters, dilated (Mode I opening) fault exposures, caves, lava tubes, or mining tunnels (Fig. 7A, B),
- Biology — tree ascents for habitat and ecosystem studies (i.e., rainforest canopies, redwoods, and other old tall forests),
- Archeology — non-destructive inspection of fragile and sensitive sites,
- Mining — search and rescue, repetitive mapping to pinpoint small changes indicative of structural failure.

In addition to the potential terrestrial application, VolcanoBot can be easily incorporated into planetary missions as a daughter robot for Lunar or Martian rovers (Fig. 7C, D). Having a deployable VolcanoBot onboard would allow a mission to extend its reach into high risk terrain unfit for the main rover, and assess sites of geological interest or as a precursor for human exploration.

Supplementary data to this article can be found online at http://dx.doi.org/10.1016/j.jvolgeores.2016.03.006.

Acknowledgments

We enthusiastically thank our reviewers Tim Orr and Don Swanson as well as the editor Lionel Wilson for their helpful and constructive feedback. We would like to thank Vladimir Arutyunov, Christine Fuller, Jesse Grimes-York, Jaakko Karras, Jonathan King, and Allen Sirota, for insightful feedback and comments on the project. We thank Alexander Menzies for providing the PrimeSense Carmine 1.09 sensors as well as Benjamin Pelletier for the assistance with the initial data processing methodology. We thank Tim Orr and the Hawaiian Volcano Observatory staff for their hospitality and logistical assistance with the fieldwork. Finally we especially thank Lionel Wilson and Linda Robshaw for their assistance in the field during VolcanoBot1 field work, and Ed Lewellin and Tom Jones for their discussions during VolcanoBot2 field work. This research was supported by an appointment to the NASA Postdoctoral Program at the Jet Propulsion Laboratory, administered by Oak Ridge Associated Universities through a contract with NASA. The research was carried out at the Jet Propulsion Laboratory, California Institute of Technology, under a contract with the National Aeronautics and Space Administration.

References

Almendros, J., Chouet, B., Dawson, P., Bond, T., 2002. Identifying elements of the plumbing system beneath Kilauea volcano, Hawai'i, from the source locations of very-long-period signals. Geophys. J. Int. 148, 303–312. http://dx.doi.org/10.1046/j.1365-246X.2002.01629.x.

Bares, J.E., Wettergreen, D.S., 1999. Dante II: technical description, results, and lessons learned. Int. J. Rob. 18 (7), 621–649. http://dx.doi.org/10.1177/02783649922066475.

Cignoni, P., Callieri, M., Corsini, M., Dellepiane, M., Ganovelli, F., Ranzuglia, G., 2008. MeshLab: an open-source mesh processing tool. Eurographics Italian Chapter Conference, pp. 129–135 (Short link: https://goo.gl/YjcIY2).

Delaney, P.T., Pollard, D.D., Ziony, J.I., McKee, E.H., 1989. Field relations between dikes and joints: emplacement processes and paleo stress analysis. J. Geophys. Res. 91 (B5), 4920–4938. http://dx.doi.org/10.1029/JB091iB05p04920.

El-laith, R.A., Huang, J., Yeh, M., 2012. Study on the use of Microsoft Kinect for robotics applications. IEEE Conference on Position Location and Navigation Symposium, pp. 1280–1288. http://dx.doi.org/10.1109/PLANS.2012.6236985.

Fisk, R.S., Koyanagi, R.Y., 1968. The December 1965 eruption of Kilauea volcano, Hawaii. US Geol. Surv. Prof. Pap. 607 (21 p. Short link: http://goo.gl/9uqjSA).

Huber, S.A., Hendrickson, D.B., Jones, H.L., Thornton, J.P., Whittaker, W.L., Wong, U.Y., 2014. Astrobotic technology: planetary pits and caves for science and exploration. Annual Meeting of the Lunar Exploration Analysis Group (Short link: http://goo.gl/cEk6iP).

Huntsberger, T., Stroupe, A., Aghazarian, H., Garrett, M., Younse, P., Powell, M., 2007. TRESSA: teamed robots for exploration and science on steep areas. J. Field Rob. 24 (11–12), 1015–1031. http://dx.doi.org/10.1002/rob.20219.

Izadi, S., Kim, D., Hilliges, O., Molyneaux, D., Newcombe, R.A., Kohli, P., Shotton, J., Hodges, S., Freeman, D., Davison, A.J., Fitzgibbon, A., 2011. KinectFusion: real-time 3D reconstruction and interaction using a moving depth camera. Proceedings of the 24th Annual ACM Symposium on User Interface Software and Technology (Short link: http://goo.gl/u0FC2X).

Konolige, K., Mihelich, P., 2012. Technical description of kinect calibration. Web reference: http://wiki.ros.org/kinect_calibration/technical.

Macdonald, G.A., Abbott, A.T., Peterson, F.L., 1983. Volcanoes in the Sea: Geology of Hawai'i. second ed. University of Hawaii Press, Honolulu.

Melexis datasheet: MLX90612, 2008. Single and dual zone infrared thermometer in T0-39 Web reference: http://www.pololu.com/file/download/MLX90614.pdf.

Muscato, G., Caltabiano, D., Guccione, S., Longo, D., Coltelli, M., Pecora, E., Cristaldi, A., Virk, G.S., Sim, P., Sacco, V., Briole, P., Semerano, A., White, T., 2013. ROBOVOLC: a robot for volcano exploration result of first test campaign. Ind. Robot. 30 (3), 231–242. http://dx.doi.org/10.1108/01439910310473942.

Nagatani, K., Akiyama, K., Yamauchi, G., Otsuka, H., Nakamura, T., Kiribayashi, S., Yoshida, K., Hada, Y., Yuta, S., Fujino, K., Izu, T., Mackay, R., 2013. Volcanic ash observation in active volcano areas using teleoperated mobile robots—introduction to our robotic-volcano-observation project and field experiments. Safety, Security, and Rescue Robots, pp. 1–6. http://dx.doi.org/10.1109/SSRR.2013.6719324.

Nesnas, I.A., Matthews, J.B., Abad-Manterola, P., Burdick, J.W., Edlund, J.A., Morrison, J.C., Peters, R.D., Tanner, M.M., Miyake, R.N., Solish, B.S., Anderson, R.C., 2012. Axel and DuAxel rovers for the sustainable exploration of extreme terrains. J. Field Rob. 29, 663–685. http://dx.doi.org/10.1002/rob.21407.

Parcheta, C.E., Houghton, B.F., Swanson, D.A., 2012. Hawaiian fissure fountains 1: decoding deposits — episode 1 of the 1969-74 Mauna Ulu eruption. Bull. Volcanol. 74, 1729–1743. http://dx.doi.org/10.1007/s00445-012-0621-1.

Parcheta, C., Fagents, S., Swanson, D.A., Houghton, B.F., Ericksen, T., 2015. Hawaiian fissure fountains: vents and shallow conduit geometry — episode 1 of the 1969-74 Mauna Ulu eruption. AGU Monogr. 208. http://dx.doi.org/10.1002/9781118872079.ch17.

Parness, A., Frost, M., Thatte, N., King, J.P., Witkoe, K., Nevarez, M., Garrett, M., Aghazarian, H., Kennedy, B., 2013. Gravity-independent rock-climbing robot and a sample acquisition tool with microspine grippers. J. Field Rob. 30 (6), 897–915. http://dx.doi.org/10.1002/rob.21476.

Point Cloud Library, 2014. Using Kinfu Large Scale to generate a textured mesh. Web Reference http://poinclouds.org/documentation/tutorials/using_kinfu_large_scale.php.

Poland, M., 2015. Points requiring elucidation about Hawaiian volcanism. AGU Monogr. 208. http://dx.doi.org/10.1002/9781118872079.ch24.

Poland, M., Hamburger, M., Newman, A., 2006. The changing shapes of active volcanoes: history, evolution, and future challenges for volcano geodesy. J. Volcanol. Geotherm. Res. 150, 1–13. http://dx.doi.org/10.1016/j.jvolgeores.2005.11.005.

Pollard, D.D., 1987. Elementary fracture mechanics applied to the structural interpretation of dykes. In: Halls, H.H., Fahrig, W.F. (Eds.), Mafic Dike Swarms Geol. Assoc. of Canada Special Paper Vol. 34, pp. 5–24 (ISBN-10: 0919216331).

Pollard, D.D., Muller, O.H., 1976. The effect of gradients in regional stress and magma pressure o the form of sheet intrusions in cross section. J. Geophys. Res. 81, 975–984. http://dx.doi.org/10.1029/JB081i005p00975.

PrimeSense Datasheet, 2013. 3D sensor design and function. Web reference http://www.robotshop.com/media/files/pdf/datasheet-sca001_1.pdf.

Raspberrypi Datasheet, 2014. Model B+. Web reference https://www.adafruit.com/datasheets/pi-specs.pdf.

Recon robotics datasheet, 2011. Web reference: http://www.reconrobotics.com/pdfs/Recon-scout_XT_spec_sheet_military.pdf.

Sharp datasheet: GP2Y0A21YK0F, 2006. Distance measuring sensor unit. Web reference: http://www.pololu.com/file/0j85/gp2y0a21yk0f.pdf (2006:E4-A00201EN).

Squyres, S.W., Knoll, A.H., 2005. Sedimentary rocks at Meridiani Planum: origin, diagenesis, and implications for life on Mars. Earth Planet. Sci. Lett. 24 (1), 1–10. http://dx.doi.org/10.1016/j.epsl.2005.09.038.

STMicroelectronis datasheet: L3G4200D, 2010. MEMS motion sensor: ultra-stable three axis digital output gyroscope. web reference: http://www.pololu.com/file/0j491/L3G4200D.pdf.

Sutoh, M., Nagaoka, K., Nagatani, K., Yoshida, K., 2012. Evaluation of influences of surface shape on locomotion mechanism on the traveling performance of planetary rovers. IEEE International Conference on Robotics and Automation, pp. 3419–3424. http://dx.doi.org/10.1109/ICRA.2012.6225024.

Swanson, D.A., Duffield, W.A., Jackson, D.B., Peterson, D.W., 1979. Chronological narrative of the 1969-1971 Mauna Ulu eruption of Kilauea volcano, Hawaii. US Geol. Surv. Prof. Pap. 1056 (Short link: http://goo.gl/xe2cjd).

Tanaka, H.K.M., Nakano, T., Takahashi, S., Yoshida, J., Takeo, M., Oikawa, J., Ohminato, T., Aoki, Y., Koyama, E., Tsuji, H., Niwa, K., 2007. High resolution imaging in the inhomogeneous crust with cosmic-ray muon radiography: the density structure below the volcanic crater floor of Mt Asama, Japan. Earth Planet. Sci. Lett. 263, 104–113. http://dx.doi.org/10.1016/j.epsl.2007.09.001.

Tilling, R.I., Christiansen, R.L., Duffield, W.A., Endo, E.T., Holcomb, R.T., Koyanagi, R.Y., Peterson, D.W., Unger, J.D., 1987. The 1972–1974 Mauna Ulu eruption, Kilauea volcano: an example of quasi-steady-state magma transfer. In: Decker, R.W., Wright, T.L., Stauffer, P.H. (Eds.), Volcanism in Hawaii. U.S. Geol. Surv. Prof. Pap. Vol. 1350(1), pp. 405–469 (Short link: http://goo.gl/jZ08AY).

Volpe, R., Balaram, J., Ohm, T., Ivlev, R., 1997. Rocky 7: a next generation Mars rover prototype. J. Advanced Robotics 11 (4), 341–358. http://dx.doi.org/10.1163/156855397X00362.

Walker, G., 1973. Explosive volcanic eruptions: a new classification scheme. Geol. Rundsch. 62, 431–446. http://dx.doi.org/10.1007/BF01840108.

Wettergreen, D., Cabrol, N., Baskaran, V., Calderon, F., Heys, S., Jonak, D., Luders, A., Pane, D., Smith, T., Teza, J., Tompkins, P., Villa, D., Williams, C., Wagner, M., 2005. Second experiments in the robotic investigation of life in the Atacama Desert of Chile. ISAIRAS Conf (Short link: https://goo.gl/qTuUX8).

Whelan, T., Johannsson, H., Kaess, M., Leonard, J.J., McDonald, J., 2012. Robust tracking for real-time dense RGB-D mapping with kintinuous. Comp. Sci. Artificial Intelligence Lab Tech Report (Short link: https://goo.gl/L4MkPG).

Wong, U., Morris, A., Lea, C., Lee, J., Whittaker, C., Barney, G., Whittaker, R., 2011. Comparative evaluation of range sensing technologies for underground void modeling. IEEE Conference on Intelligent Robots and Systems (Short link: http://goo.gl/QicZjv).

Wylie, J.J., Helfrich, K.R., Dade, B., Lister, J.R., Salzig, J.F., 1999. Flow localization in fissure eruptions. Bull. Volcanol. 60 (6), 423–440. http://dx.doi.org/10.1007/s004450050243.

Yajima, R., Nagatani, K., Yoshida, K., 2014. Development and field testing of UAV-based sampling devices for obtaining volcanic products. Safety, Security, and Rescue Robots, pp. 1–5. http://dx.doi.org/10.1109/SSRR.2014.7017680.